UPDATED JET FLAME RADIATION MODELING WITH BUOYANCY CORRECTIONS

Ekoto, I.W.[1], Ruggles, A.J.[1], Creitz, L.W.[2], and Li, J.X.[2]
[1]Sandia National Laboratories, Livermore, CA 94551-0969, USA, ajruggl@sandia.gov
[2]Air Products and Chemicals Inc., Allentown, PA 18105, USA

ABSTRACT

Radiative heat fluxes from small to medium-scale hydrogen jet flames (< 10 m) compare favorably to theoretical predictions provided the product species thermal emittance and optical flame thickness are corrected for. However, recent heat flux measurements from two large-scale horizontally orientated hydrogen flames (17.4 and 45.9 m respectively) revealed that current methods underpredicted the flame radiant fraction, defined as the radiative energy escaping relative to chemical energy released, by 40% or more. Newly developed weighted source flame radiation models have demonstrated substantial improvement in the heat flux predictions, particularly in the near-field, and allow for a sensible way to correct potential ground surface reflective irradiance. These updated methods are still constrained by the fact that the flame is assumed to have a linear trajectory and flame, despite buoyancy effects that can result in significant flame deformation. The current paper discusses a method to predict flame centerline trajectories via a one-dimensional integral model, which enables optimized placement of source emitters for weighted multi-source heat flux prediction methods. Flame shape prediction was evaluated against flame envelope imaging and was found to depend heavily on the notional nozzle model formulation used to compute the density weighted effective nozzle diameter. Nonetheless, substantial improvement in the prediction of downstream radiative heat flux values occurred when emitter placement was corrected by the flame integral, regardless of the notional nozzle model formulation used.

1.0 INTRODUCTION

A primary hazard associated with the unintended release and subsequent ignition of hydrogen from storage, transport, and delivery applications is radiant heat flux exposures and elevated temperatures from hydrogen jet flames that can result in potentially lethal burns and severe respiratory damage [1]. Detailed flame simulations have provided useful information about the interplay between flow dynamics and combustion chemistry [2, 3], but are prohibitive for practical safety applications due to the significant computational resources required. Reduced order models developed from empirical observation are often used instead to determine hazard boundaries [4-11]. These models require relevant release conditions (e.g., nozzle diameter/shape, mass flow rate, gas type) to estimate flammable envelopes and the amount of flame energy converted into escaping radiant energy, defined here as the radiant fraction, χ. Schefer et al. [12] reported that as with hydrocarbon flames, laboratory scale hydrogen jet flame radiant fractions exhibit a logarithmic dependence on flame residence time in, t_f, although the absence of CO_2 or soot in the product stream results in overall lower radiant fractions [13]. Based on these observations, Molina et al. [14] developed a unified expression that treated the flame as a blackbody emitter with radiant fraction expressed a function of flame residence time, adiabatic flame temperature ($T_{ad,H2}$ = 2390 K), and Plank's mean absorption coefficient for the product species ($a_{f,H2O}$ = 0.23 m^{-1}).

Eq. 1. $$\chi = 0.08916 \cdot log_{10}\left(t_f a_f T_{ad}^4\right) - 1.2172$$

Note that the flame residence time is in milliseconds. Nonetheless, a gap remains between computationally expensive simulations and low-fidelity empirical models that have limited applicability in realistic scenarios. To bridge this gap, Air Products and Chemicals Inc. commissioned radiative heat flux measurements from two large-scale hydrogen flames that issued from large pressurized reservoirs. They then worked with Sandia National Laboratories' Hydrogen Safety, Codes and Standards research group to analyze the results and develop improved modeling approaches. Initial radiant heat flux predictions derived from conventional single point source models [6, 11] were

underpredicted measured values by 40% or more, particularly in the near-field. For most locations, the difference was accounted for if multi-source models were used and reflective surface addition from steel and concrete below the release path was included [15]. The exception was from a radiometer placed directly downstream of the expected flame length, which recorded radiative heat fluxes far below the model predictions. It was noted that curved centerline flame trajectories due to buoyancy effects were not captured and may have increased optical path lengths between the flame and radiometer. The present paper discusses the development of a one-dimensional flame integral model to predict flame centerline trajectories, which is then used to optimize the emitter source placement. Model entrainment coefficients were calibrated from detailed flame velocity and scalar data and model performance was evaluated against large-scale horizontally propagating hydrogen jet flame images.

2.0 LARGE-SCALE FLAME EXPERIMENTS

Two large-scale hydrogen jet fire experiments were conducted at the GL Noble Denton Spadeadam Test Site in North Cumbria, UK. Compressed hydrogen gas was released from a nominal 60 barg stagnation pressure through a horizontally orientated 1 m long stretch of pipe with respective internal diameters of 20.9 mm (1) and 52.5 mm (2), and located 3.25 m above the ground. Boundary and ambient condition details for each test are summarized in Table 1 while images of the release setup and delivery system schematic are given in Figure 1. Since the storage and delivery lines had previously been used for similar tests of natural gas flames, 3 consecutive hydrogen purges were performed prior to the experiments to remove any residual natural gas from the system. A 25 m by 15 m concrete pad below the release path was used to prevent surface dirt entrainment into the flame. To protect against spallation, the pad was further covered with steel sheeting.

Table 1. Boundary and ambient conditions for each large-scale jet flame. Note that wind directions are where the wind is coming from relative to true north while the release direction is the direction of the release path.

Flame	d_j[mm]	$\dot{m}$ [kg/s]	p_0 [barg]	T_0 [K]	RH [%]	T_{amb} [K]	p_{amb} [bar]	u_{wind} [m/s]	φ_{wind} [°]	L_{vis} [m] (rms)
1	20.9	1.0	59.8	308.7	94.3	280	1.022	2.84	68.5	17.4 (1.1)
2	52.5	7.4	62.1	287.8	94.5	280	1.011	0.83	34.0	45.9 (2.5)

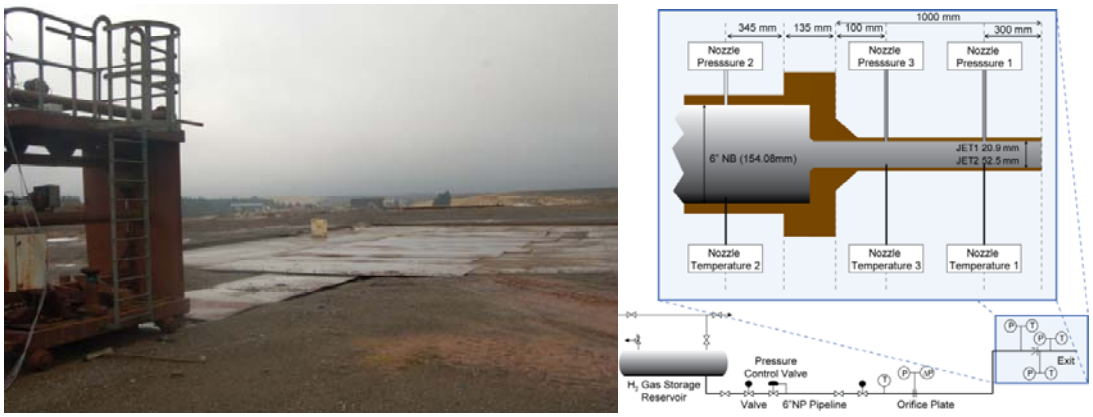

Figure 1. Image of the pipe release setup at the GL Noble Denton Spadeadam Test Site (left) and a schematic of the storage reservoir and release setup (right).

Mass flow rates were calculated from upstream temperature measurements and the pressure drop across an orifice plate in accordance with ISO 5167 parts 1 and 2 [16]. Orifice pressure drop and static temperature were respectively measured by a Druck STX 2100 differential pressure transducer (0 – 2.0 bar range, 0.2% full-scale accuracy) and a type 'T' thermocouple with outputs linearized by a Pretop 5331B temperature transmitter (±100°C, 0.05% full-scale accuracy). Static pressure and temperature were measured at three release pipe locations via Druck PTX-1400 pressure transducers

(0–100 barg range, 0.15% full-scale accuracy) and the same thermocouple systems used for upstream mass flow rate measurements. Incident thermal radiation was measured by a wide-angle Medtherm radiometer (150° field of view, 0.3 – 11.5 μm transmission, 1.0 second response time, ±5% full-scale accuracy) that was mounted on a tripod and orientated towards the projected flame center; radiometer positions for both flames are given in Table 2 and a schematic in Figure 2 illustrates the placement.

Table 2. Jet flame radiometer positions relative to the release exit for each test along the horizontal distance of the predicted flame center from the release point, which is where the radiometers were orientated towards.

	x [m]	y [m]	z [m]	Predicted Flame Center Distance from Release [m]
Flame 1	26.0	1.75	0.0	11
Flame 2	48.0	1.75	0.0	23

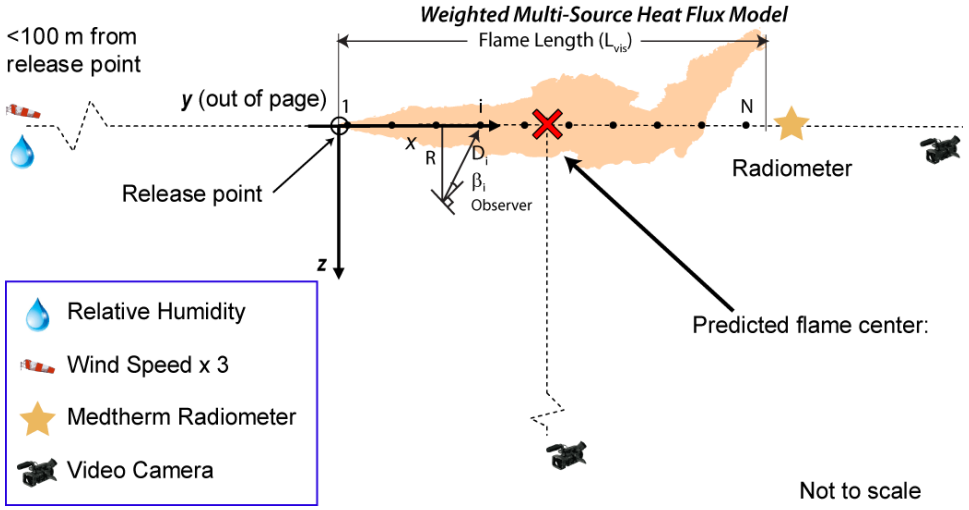

Figure 2. Radiometer and camera placement schematic relative to the jet flame release point along with a conceptual illustration of the weighted multi-source model.

Flame envelopes were recorded by 2 standard definition cameras positioned perpendicular to the cross and downstream field of views (see Figure 2). Visible flame lengths were established by averaging maximum visible extents from each cross stream video image, with standard deviations reported in Table 2. Wind speed/direction, ambient temperature, and relative humidity were measured at a weather tower located ~111 m upstream from the release point. Ambient pressure was reported from a nearby weather station located at Carlisle, Cumbria, UK. The flames were oriented 67° relative to true north. Further details about test setup and operating procedures can be found in Ekoto et al. [15] — note that in [15] the flame length for the larger release was reported at 48.5 m, which corresponded to the maximum observed flame length rather than the average value of 45.9 m as reported here.

3.0 WEIGHTED MULTI SOURCE FLAME RADIATION MODEL

Observer heat flux is proportional to the view factor, *VF*, or the viewable portion of radiant emission, atmospheric transmissivity, τ, and surface emissive power, *S*:

Eq. 2. $q = VF \cdot S \cdot \tau$, where $S = \chi \cdot \dot{m} \cdot \Delta H_c$

Here, $\dot{m}$ is the mass flow rate, and ΔH_c is the gas heat of combustion (= 119 MJ/kg for H_2). Atmospheric transmissivity was expressed by simple Beer-Lambert expressions that account for the H_2O concentration in the view path [17]. Hankinson and Lowesmith [10] recently developed a

weighted multi-source model that was found to have good near-field agreement with heat flux measurements; the transmission corrected view factor-to-surface area ratio was expressed as:

Eq. 3. $\tau\frac{VF}{A_f}=\sum_{i=1}^{N}\frac{w_i cos\,\beta_i}{\pi D_i^2}\tau_i$, where $w_i=\begin{cases} iw_1 & i\le 0.75N \\ \left[n-\frac{n-1}{N-n-1}(j-n+1)\right]w_1 & i>0.75N \end{cases}$; $\sum_{i=1}^{N}w_i=1$

Here, D and β are respectively the distance and angle between the observer unit normal and the point emitter, while w is an emitter strength weighting parameter. A total of 80 source emitters, selected based on a convergence study as part of the work in [15], were evenly distributed from the jet exit up to the projected visible flame length along the flame centerline.

To estimate flame residence time for the radiant fraction calculation in equation 1, the model by Turns and Myhr [13] that relates residence time to fuel mass flow rates and flammable volumes was used:

Eq. 4. $t_f=\frac{\pi}{12}\frac{\rho_f\cdot W_f^2\cdot L_f Y_s}{\dot{m}}$; where $\rho_f=\frac{p_{amb}MW_{st}}{RuT_{ad}}$

Here, Y_s, is the hydrogen stoichiometric mass fraction, ρ_f is the flame density, p_{amb} is ambient pressure, MW_{st} is the stoichiometric molecular weight, and Ru is the universal gas constant. The visible flame length, L_f , and width, W_f, were estimated from correlations by Delichatsios [18] where:

Eq. 5. $L_f=\frac{L^*\cdot}{Y_s}d^*$ and $W_f\approx 0.17L_f$

The non-dimensional flame length, L^*, was expressed as a function of the flame Froude number:

Eq. 6. $L^*=\begin{cases}\frac{13.5Fr_f^{0.4}}{\left(1+0.07Fr_f^2\right)^{0.2}} & for\ Fr_f<5 \\ L^*=23 & for\ Fr_f\ge 5\end{cases}$ where, $Fr_f=\frac{u_{eff}Y_s^{1.5}}{\left(\frac{\rho_{eff}}{\rho_{amb}}\right)^{0.25}\left(\frac{T_{ad}-Tamb}{T_{amb}}.g\cdot d_{eff}\right)^{0.5}}$

The visible flame length of equation 5 was proportional to the mass weighted effective diameter, d^* ($\equiv d_{eff}\sqrt{\rho_{eff}/\rho_{amb}}$) [19], where d_{eff} and ρ_{eff} were the jet exit diameters and densities derived from pseudo source models that account for complex jet-exit shock structure. For the present study, 4 source models were examined. Each model preserved mass and energy conservation [20, 21], and successively added momentum [12, 22] and entropy conservation across a normal shock [23] to reduce the number of assumed boundary conditions. Note that the Birch et al. [20] and Harstad and Bellan [23] models were updated with the Abel-Noble equation of state as described by Ruggles and Ekoto [24] to account for real gas effects.

4.0 FLAME INTEGRAL MODEL

A flame integral model was used to determine centerline trajectories that resulted from external body and surface forces (e.g., buoyancy and wind), with only buoyancy considered here for brevity. For the flame integral model, the conservation equations for mass, momentum, and mixture fraction, f, were integrated over the flame cross-sectional area and differentiated along the flame centerline; a schematic is provided in Figure 3.

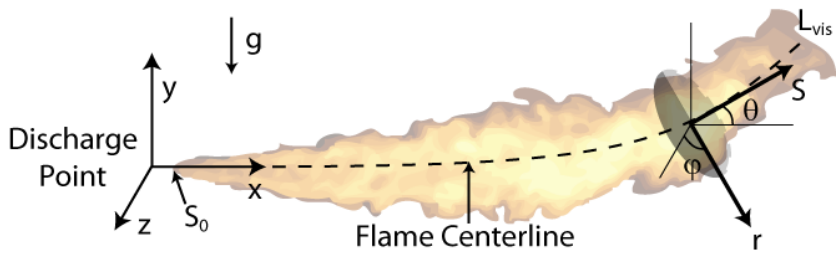

Figure 3. Schematic of the one-dimensional buoyant jet flame model.

Mixture fraction was used in lieu of species mass fraction since it is a conserved scalar with the form:

Eq. 7. $$f = \frac{MW_{H_2}(\chi_{H_2}+\chi_{H_2O})}{MW} = Y_{H_2} + Y_{H_2O}\frac{MW_{H_2}}{MW_{H_2O}}$$

The flame was assumed to issue from the origin at some arbitrary angle, ($\theta_0 = 0$ for the present flames). Initial conditions were specified by the notional nozzle models referred in Section 3 and the parameters from Table 1 for both flames. The zone of flow establishment between the notional nozzle and established flow zones was modeled following the method described by Winters [25] for an unignited buoyant jet, under the assumption that the jet ignited at the end of this zone. The established flow zone began at point S_0, with the centerline flame axis given by the streamline coordinates S and θ. Radial distances perpendicular to S and the azimuthal angle about S were designated r and φ respectively. Gravity, g, was parallel to the vertical (y-axis) and directed downward. Integral flame conservation equations were as follows:

Eq. 8. $$\frac{d}{dS}\int_0^{2\pi}\int_0^{\infty}\rho V r dr d\phi = \rho_{amb}E$$ (mass conservation)

Eq. 9. $$\frac{d}{dS}\int_0^{2\pi}\int_0^{\infty}\rho V^2\cos\theta\, r dr d\phi = 0$$ (x-momentum conservation)

Eq. 10. $$\frac{d}{dS}\int_0^{2\pi}\int_0^{\infty}\rho V^2\sin\theta\, r dr d\phi = \int_0^{2\pi}\int_0^{\infty}(\rho_{amb}-\rho) g r dr d\phi$$ (y-momentum conservation)

Eq. 11. $$\frac{d}{dS}\int_0^{2\pi}\int_0^{\infty}\rho V f r dr d\phi = 0$$ (mixture fraction conservation)

Eq. 12. $$\frac{dx}{dS} = \cos(\theta)$$ (x-centerline coordinate)

Eq. 13. $$\frac{dy}{dS} = \sin(\theta)$$ (y-centerline coordinate)

Here V and ρ were the local time averaged velocity and density respectively, ρ_{amb} was the ambient air density, x and y were the flame centerline coordinates, and E is the local ambient entrainment rate. Measurements by Cheng et al. [26], Barlow et al. [27], and Flury and Schlatter [28] indicated radial mixture fraction and velocity profiles were nearly Gaussian and thus could be expressed as:

Eq. 14. $$f = f_{cl}\exp\left(-\frac{r^2}{\lambda_f^2 B^2}\right)$$

Eq. 15. $$V = V_{cl}\exp\left(-\frac{r^2}{\lambda_V^2 B^2}\right)$$

where V_{cl} and f_{cl} were the time-averaged centerline values velocity and mixture fraction, r was the radial coordinate, and B was the characteristic jet width. The respective mixture fraction and velocity spreading ratios relative to B were given by λ_f and λ_V. It was noted by Cheng et al. [26] that radial velocity and mixture fraction profiles had similar spreading ratios; accordingly the reported value ($\lambda = 1.24$) was used for both.

Although significant endothermic chemical reaction resulted, energy conservation was not explicitly calculated. Instead, the mixture was assumed to be thermally perfect with the local enthalpy, h, expressed as a function of the ambient enthalpy, h_{amb}, the hydrogen heat of combustion ΔH_c (= 119MJ/kg), and the local composition:

Eq. 16. $$h = C_p(T)T = h_{amb}\frac{\rho_{amb}}{\rho} + \Delta H_c\left(f - Y_{H_2}\right)$$

Radial mixture composition and temperature, T, were iteratively computed from equations 14 and 16, under the assumption that the mixture was in chemical equilibrium. Temperature and mixture composition were then used to specify the local density in equations 8 – 11.

To model local entrainment, the approach by Houf and Schefer [29] was adopted where the turbulent entrainment rate, E, was composed of momentum, E_{mom} [30], and buoyancy, E_{buoy} [31], components.

Eq. 17. $E = E_{mom} + E_{buoy};\ E_{mom} = \alpha_m \left(\frac{\pi D_{exit}^2}{4}\frac{\rho_{exit}V_{exit}^2}{\rho_{amb}}\right)^{\frac{1}{2}};\ E_{buoy} = 2\pi\alpha_b \sin\theta \frac{g\left(\rho_{amb} - \int_0^B \rho dr\right)}{V_{cl}\rho_{exit}}$

Since centerline density was not normally distributed, the integrated density bounded by the jet half-width was used instead. Equation 17 indicates momentum dominates the initial jet development, while buoyancy forces strengthen as centerline velocities decrease; observations that qualitatively agree with flame imaging from Ekoto et al. [15]. Entrainment rate constants α_m (= 0.040) and α_b (= 0.00125) were empirically determined from *in situ* scalar and velocity measurements [27, 28] of a vertical turbulent hydrogen jet flame with a 3.75 mm diameter source and exit Reynolds number of 10,000.

Equations 14 – 17 were applied to the conservation equations (8 – 13), with differentials of the 6 independent variables (V_{cl}, f_{cl}, B, θ, x, and y) brought outside of the integral. The remaining radially dependent terms were numerically solved via the trapezoid rule (3,000 uniform steps and an upper radial limit of 6B). Larger limits and smaller step sizes did not appreciably change the numerical results. The independent variables were simultaneously solved at each discrete S location via the Matlab ODE45 routine. Mean velocity and mixture fraction measurements from [27, 28] were collapsed onto non-dimensional radial coordinates in Figure 4 and compared to the Gaussian fit from Cheng et al. [26]; good agreement was observed for both statistics. Also compared in Figure 4 are centerline velocity and mixture fraction measurements from the same studies relative to the flame integral model predictions. Again, the match for both statistics was excellent and the general behavioral was well captured.

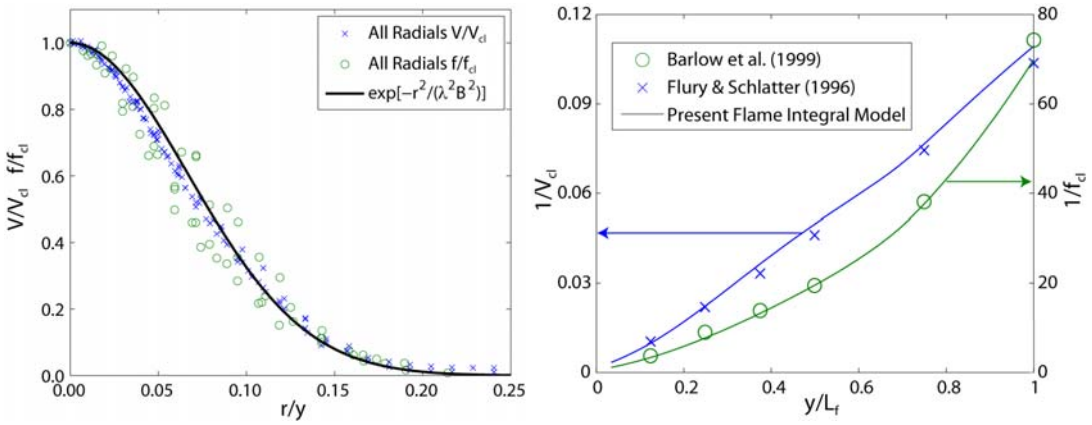

Figure 4. Collapsed mean velocity and mixture fraction [27, 28] measurements compared to the radial fit from Cheng et al. [26] (right), along with measured centerline velocity and mixture fraction decay rates relative to the flame integral model results (left).

5.0 LARGE-SCALE FLAME RESULTS AND DISCUSSION

Representative still images from the standard video recordings of the two large-scale jet flames described in Section 2 are provided in Figure 5 along with a comparison of the projected centerline trajectories produced from the integral model and the 4 pseudo source models described in Section 3. Significant centerline trajectory curvature was observed for both flames beyond the midpoint, and this qualitative behavior was well captured by the integral model regardless of the pseudo source formulation used. It is interesting to note that the most complete pseudo source model (Harstad and Bellan [23]) vastly over-predicted flame curvature for both flames while the simpler model by Schefer et al. [12] that neglected entropy conservation at the Mach disk under-predicted flame path curvature. However, the simplest models by Birch et al. [20] and Molkov et al. [21], which also neglected momentum conservation, best captured the visible centerline flame path.

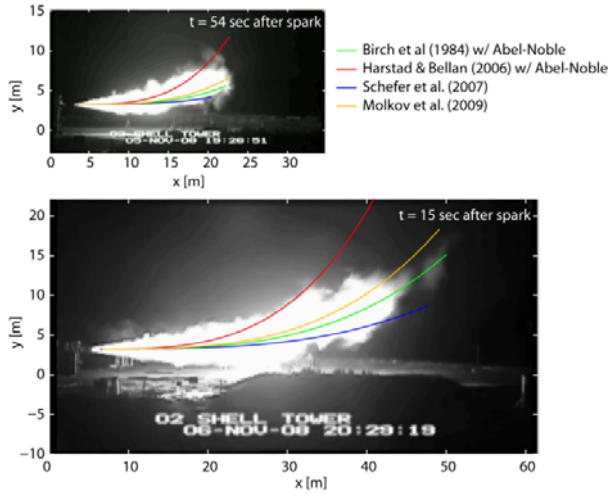

Figure 5. Comparison of flame integral model centreline trajectories with 4 pseudo source models for the large-scale flames (20.9 and 52.5 mm release diameters) with a 60 barg source pressure.

Projected visible flame lengths and downstream radiative heat fluxes from the "straight" (i.e., linear) flame paths or from "curved" flame paths specified by the integral model are tabulated in Table 3 along with the measured values. For the smaller flame (20.9 mm source diameter), the flame length was well predicted by all input pseudo source models except for Harstad and Bellan. Ruggles and Ekoto [24] noted this model tends to over-predict effective source diameters, and hence flammable extents, due to the faulty assumption that all fluid passes through the Mach disk. Accordingly, the predicted radiative heat flux from the "straight" flame was nearly 3 times higher than the measured value since the sensor was predicted to reside within the flame envelope. To a lesser degree, the Molkov et al. and Birch et al. models also over-estimated visible flame lengths, and hence radiative heat fluxes if no flame curvature was assumed. However, when source emitter placement was adjusted by centerline flame curvature, predicted heat fluxes more closely approached the measured values.

Table 3. Visible flame length and radiative heat flux predictions from 4 separate pseudo source models for the large-scale flames (20.9 and 52.5 mm release diameters) with a 60 bar source pressure. Source emitters for equation 3 were placed along the centerline, with trajectories specified either by the straight flame assumption or the new flame integral model.

Pseudo Source Model (Flame 1)	L_f [m]	q_{rad} (Straight Flame) [kW/m^2]	q_{rad} (Curved Flame) [kW/m^2]
Measurement	17.4	–	4.7
Birch et al. (1984) w/ Abel-Noble	19.7	6.6	6.2
Schefer et al. (2007)	17.5	4.6	4.5
Harstad & Bellan (2006) w/ Abel-Noble	23.1	12.5	6.6
Molkov et al. (2009)	20.2	7.3	6.5

Pseudo Source Model (Flame 2)	L_f [m]	q_{rad} (Straight Flame) [kW/m^2]	q_{rad} (Curved Flame) [kW/m^2]
Measurement	45.9	–	23.9
Birch et al. (1984) w/ Abel-Noble	49.2	77.9	26.6
Schefer et al. (2007)	44.6	30.2	24.9
Harstad & Bellan (2006) w/ Abel-Noble	52.5	164.9	14.4
Molkov et al. (2009)	49.9	92.6	23.1

For the larger flame, visible flame length predictions for all source models were within ±10% of the measured values. Contours that correspond to the 2012 International Fire Code (IFC) exposure limits for property lines (1.577 kW/m^2), employees (4.732 kW/m^2), and non-combustible equipment (25.237 kW/m^2) [32] are displayed in Figure 6 along with the projected flame centerline and sensor location (asterisk). The upper left plot of the "straight" flame with the Schefer et al. pseudo source model indicates that — in contrast to the measurements — the sensor resided within the elevated heat flux boundary of even the smallest predicted flame envelope, with heat flux predictions from the other source models considerably worse. However, when flame curvature was considered, the heat flux predictions from most pseudo source models were in excellent agreement with the measurements as flame curvature directed the heat flux boundary upward and away from the observer on the ground. Note however, that the severe curvature from the flame integral model with the Harstad and Bellan source model as the input led to significantly under-predictions of radiative heat flux values. Finally, it should be noted that results from crosswind sensors located near the projected flame half-width and at discrete radial locations (see Ekoto et al. [15] for further details) were also evaluated. However, there was no appreciable change in predicted radiative heat flux values with source placement via the linear or curved flame trajectories, since the strongest curvature happened downstream of these measurements. Hence, these results were excluded from the current analysis.

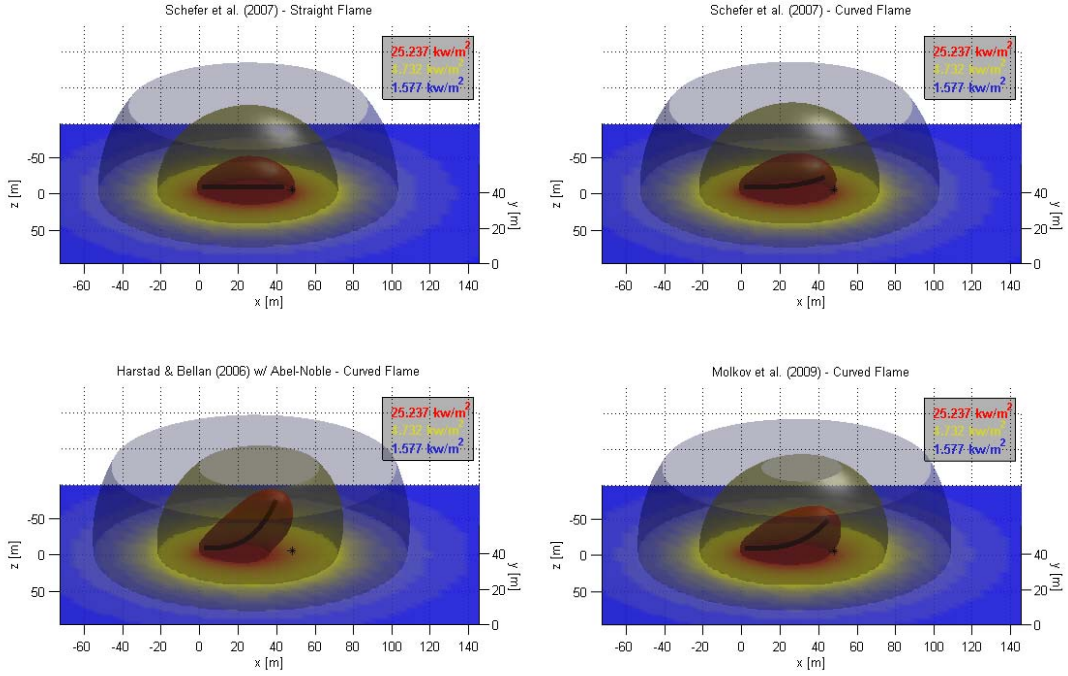

Figure 6. Predicted radiative heat flux contours at different IFC exposure limits from the largest flame (52.5 mm diameter, 60 barg). Emitter placement was specified by the "straight" flame assumption with the Schefer et al. source model (top left) and the integral flame model with the Schefer et al. (top right), Harstand and Bellan (bottom left), and Molkov et al. (bottom right) source models.

6.0 CONCLUSIONS

A new flame integral model was developed to account for flame centerline trajectory distortion by buoyancy effects. The model was based on the observation that velocity and mixture fraction radial profiles collapsed to a uniform Gaussian profile when appropriately scaled. Centerline statistical quantities and trajectories were calculated from a differential solver along with numerical integration of the radially dependent quantities of the conservation equations. Mixture compositions were specified from the local mixture fraction and the assumption that the flame was in chemical

equilibrium. Local air entrainment rate was split into momentum and buoyancy dominated terms, with entrainment rate coefficients for each component specified from high-fidelity turbulent hydrogen flame scalar and velocity data.

The flame integral model was used to predict downstream flame trajectories for 2 large-scale hydrogen jet flames (20.9 and 52.5 mm internal diameters) with nominal 60 barg source pressures. Mass weighted effective source diameters used to calculate flame lengths and integral model input boundary conditions were computed by 4 different pseudo source models of varying complexity. Predicted flame trajectories were found to be highly dependent on the pseudo source model used for input boundary conditions. Relative to the flame imaging, the most complex model by Harstad and Bellan that accounted for mass, momentum, energy, and entropy conservation over-estimated flame curvature, while the simpler model by Schefer et al. that neglected entropy conservation across the normal shock underestimated flame path curvature. The Birch et al. and Molkov et al. that further neglected momentum conservation were found to produce path trajectories that best agreed with the imaging data. Research is ongoing as to why the simpler models performed best, but the current theory is that the assumption that all fluid passes through the Mach disk is faulty and needs to be revisited.

Radiative heat flux boundaries were predicted using a weighted multi-source model with source emittance tuned by radiant fraction correlations. Source emitter location was specified by either assuming a conventional linear trajectory or by placing the emitter along the predicted flame centerline path from the integral flame model. Downstream radiative heat flux predictions were substantially improved relative to the measurements when flame curvature was accounted for, regardless of the notional nozzle model used, as this increased the distance between the observer and the flame envelope. These results demonstrate the efficacy of the flame integral model, which can be an effective tool to reduce separation distances for flames expected to have large buoyancy components.

7.0 ACKNOWLEDGMENTS

This research was supported by the United States Department of Energy Fuel Cell Technologies Office, under the Safety, Codes, and Standards subprogram element managed by Will James. Sandia is operated by the Sandia Corporation, a Lockheed Martin Company, for the U.S. DOE under contract No. DE-AC04-94-AL8500. The authors gratefully acknowledge Michael Acton from GL Noble Denton and Barbara Lowesmith from Hazard Analysis Ltd. for acquisition and analysis of the original datasets along with productive discussions regarding follow-on interpretation of experimental results.

8.0 REFERENCES

[1] LaChance J, Tchouvelev A, Engebo A, Development of uniform harm criteria for use in quantitative risk analysis of the hydrogen infrastructure. Int J Hydrogen Energy, 2011;36:59-66.

[2] Coelho PJ, Numerical simulation of radiative heat transfer from non-gray gases in three-dimensional enclosures. J Quant Spectrosc Ra, 2002;74:307-28.

[3] Richardson ES, Yoo CS, Chen JH, Analysis of second-order conditional moment closure applied to an autoignitive lifted hydrogen jet flame. P Combust Inst, 2009;32:1695-703.

[4] Chamberlain GA, Developments in Design Methods for Predicting Thermal-Radiation from Flares. Chem Eng Res Des, 1987;65:299-309.

[5] Johnson AD, Brightwell HM, Carsley AJ, A Model for Predicting the Thermal-Radiation Hazards from Large-Scale Horizontally Released Natural-Gas Jet Fires. Process Saf Environ, 1994;72:157-66.

[6] Sivathanu YR, Gore JP, Total Radiative Heat-Loss in Jet Flames from Single-Point Radiative Flux Measurements. Combust Flame, 1993;94:265-70.

[7] API 521, Guide for Pressure-Relieving and Depressuring Systems, 4th edition, American Petroleum Institute, 1997.

[8] Cook DK, Fairweather M, Hammonds J, Hughes DJ, Size and Radiative Characteristics of Natural-Gas Flares .1. Field Scale Experiments. Chem Eng Res Des, 1987;65:310-7.

[9] Lowesmith BJ, Hankinson G, Acton MR, Chamberlain G, An overview of the nature of hydrocarbon jet fire hazards in the oil and gas industry and a simplified approach to assessing the hazards. Process Saf Environ, 2007;85:207-20.
[10] Hankinson G, Lowesmith BJ, A consideration of methods of determining the radiative characteristics of jet fires. Combust Flame, 2012;159:1165-77.
[11] Houf W, Schefer R, Predicting radiative heat fluxes and flammability envelopes from unintended releases of hydrogen. Int J Hydrogen Energy, 2007;32:136-51.
[12] Schefer RW, Houf WG, Williams TC, Bourne B, Colton J, Characterization of high-pressure, underexpanded hydrogen-jet flames. Int J Hydrogen Energy, 2007;32:2081-93.
[13] Turns SR, Myhr FH, Oxides of Nitrogen Emissions from Turbulent Jet Flames - .1. Fuel Effects and Flame Radiation. Combust Flame, 1991;87:319-35.
[14] Molina A, Schefer RW, Houf WG, Radiative fraction and optical thickness in large-scale hydrogen-jet fires. P Combust Inst, 2007;31:2565-72.
[15] Ekoto IW, Houf WG, Ruggles AJ, Creitz LW, Li JX, Large-Scale Hydrogen Jet Flame Radiant Fraction Measurements and Modeling. Proc International Pipeline Conference, Calgary, Canada, Sept 24-28, 2012.
[16] ISO 5167, Measurement of fluid flow by means of pressure differential devices inserted in circular cross-section conduits running full, International Standards Organization, Geneva, Switzerland, 2003.
[17] Wayne FD, An Economical Formula for Calculating Atmospheric Infrared Transmissivities. J Loss Prevent Proc, 1991;4:86-92.
[18] Delichatsios MA, Transition from Momentum to Buoyancy-Controlled Turbulent Jet Diffusion Flames and Flame Height Relationships. Combust Flame, 1993;92:349-64.
[19] Thring MW, Newby MP, Combustion length of enclosed turbulent jet flames. P Combust Inst, 1953;4:789-96.
[20] Birch AD, Brown DR, Dodson MG, Swaffield F, The Structure and Concentration Decay of High-Pressure Jets of Natural-Gas. Combust Sci Technol, 1984;36:249-61.
[21] Molkov VV, Makarov DV, Bragin MV, Physics and modelling of underexpanded jets and hydrogen dispersion in atmosphere. Proc 24th International Conference on Interaction of Intense Energy Fluxes with Matter, Elbrus, Mar 1-6, 2009.
[22] Birch AD, Hughes DJ, Swaffield F, Velocity Decay of High-Pressure Jets. Combust Sci Technol, 1987;52:161-71.
[23] Harstad K, Bellan J, Global analysis and parametric dependencies for potential unintended hydrogen-fuel releases. Combust Flame, 2006;144:89-102.
[24] Ruggles AJ, Ekoto IW, Ignitability and mixing of underexpanded hydrogen jets. Int J Hydrogen Energy, 2012;37:17549-60.
[25] Winters WS, Modeling Leaks from Liquid Hydrogen Storage Systems. SAND Report 2009-0035, Sandia National Laboratories, 2009.
[26] Cheng TS, Wehrmeyer JA, Pitz RW, Simultaneous Temperature and Multispecies Measurement in a Lifted Hydrogen Diffusion Flame. Combust Flame, 1992;91:323-45.
[27] Barlow RS, Smith NSA, Chen JY, Bilger RW, Nitric oxide formation in dilute hydrogen jet flames: Isolation of the effects of radiation and turbulence-chemistry submodels. Combust Flame, 1999;117:4-31.
[28] Flury M, Schlatter M, Laser Doppler Velocimetry Measurements in Turbulent Non-Premixed Hydrogen/Helium Flames. 1996. Available from: http://www.sandia.gov/TNF/DataArch/H2HeData.html.
[29] Houf W, Schefer R, Analytical and experimental investigation of small-scale unintended releases of hydrogen. Int J Hydrogen Energy, 2008;33:1435-44.
[30] Ricou FP, Spalding DB, Measurements of Entrainment by Axisymmetrical Turbulent Jets. J Fluid Mech, 1961;11:21-32.
[31] Hirst EA, Analysis of buoyant jets within the zone of flow establishment. Report ORNL-TM-3470, Oak Ridge National Laboratory, 1971.
[32] International Fire Code, International Code Council, Country Club Hills, IL, 2012.